npj | advanced manufacturing

Article

https://doi.org/10.1038/s44334-026-00069-w

# Hydrogen-based ore-to-part manufacturing of near-net-shape stainless steel

Check for updates

**Mingzhang Yang**[1,2], **Rangasayee Kannan**[3], **Mohsen K. Keshavarz**[1] & **Mihaela Vlasea**[1] ✉

Decarbonizing iron and steelmaking, combined with global disruptions to raw material supply chains, necessitates novel approaches to iron and steel production. In this work, we demonstrate a direct ore-to-part manufacturing route using a mixture of ore-derived oxide powders of $Fe_2O_3$, $Cr_2O_3$, NiO, and $MoO_3$ as feedstock for additive manufacturing, combined with sintering under $H_2$ to produce a near-net-shape austenitic stainless-steel. Complete reduction of all constituent oxides, including $MoO_3$ and $Cr_2O_3$, is achieved in-situ at 1300 °C, resulting in dense, crack-free bulk alloy. The fabricated part retains geometric fidelity while undergoing substantial volumetric shrinkage inherent to redox and sintering. Thermodynamic calculations elucidate the co-reduction mechanisms and alloying pathways that enable complete metallization. This work is the first demonstration of net-shaping metal parts directly from ore derived oxides, and this ore-to-part approach can minimize the emissions and lead time for manufacturing associated with downstream processing such as rolling, forging, and machining.

The synthesis and processing of metals is the largest source of greenhouse gas emissions[1]. Most metals occur in the Earth's crust as mixed oxides or sulfides, traditionally extracted via energy-intensive pyrometallurgical reduction using fossil-based agents (e.g., coke, coal), releasing $CO_2$[1]. This approach is predominant for recovering transition metals such as iron, nickel, copper, chromium, cobalt, manganese, zinc, and tin from their oxidized forms[2]. After extraction, additional processing is needed to produce application-ready parts, including liquid alloying, thermomechanical treatment (e.g., forging, rolling), machining, or shaping through extrusion or atomization followed by powder metallurgy or additive manufacturing. Thus, starting from extraction all the way to the final part production has their associated energy footprint thereby negatively impact economic sustainability.

$H_2$-based redox reactions have emerged as a sustainable alternative to fossil reductant-based extraction, oxidizing $H_2$ to $H_2O$ rather than $CO_2$, directly supporting decarbonization[3]. Vacancy formation during $H_2$ redox promotes atomic interdiffusion, enabling solid-state alloying and mass transport for densification. Recent studies have demonstrated alloying from mixed oxides (e.g., Fe-, Ni-, Cu-, Co-, Mo-, Cr-oxides), but under idealized conditions: nano-sized, high-purity powders shaped into micro-lattices and free from naturally occurring gangue oxides such as silicates ($SiO_2$) and alumina ($Al_2O_3$)[4–6]. In practice, gangue is inevitably present in industrial ores[7]; removing these gangues via separation or hydrometallurgy incurs substantial environmental costs. To realize the full potential of $H_2$-based metallurgy at scale, two fundamental questions must be answered: (1) firstly, whether near-net-shape bulk components can be directly synthesized and (2) secondly, how trace gangue oxides influence alloying behavior and final microstructure. Resolving these questions is critical for advancing $H_2$-based metallurgy toward industrial-scale, sustainable implementation.

To this end, we investigate a sustainable manufacturing paradigm: net-shaping of bulk alloy parts directly from mixed transition metal oxides through $H_2$-based redox alloying, without extensive purification. This approach is demonstrated by manufacturing austenitic stainless steel one of the ubiquitous alloys with wide range of applications, while deliberately retaining realistic gangue levels. A suspension front bearing serves as a demonstrator to assess the feasibility of net-shaping. Furthermore, we

---

[1]Multi-scale Additive Manufacturing Laboratory, University of Waterloo, Waterloo, ON, Canada. [2]Fraunhofer Institute for Manufacturing Technology and Advanced Materials, Dresden, Saxony, Germany. [3]Manufacturing Science Division, Oak Ridge National Laboratory, Oak Ridge, TN, USA. Notice of Copyright: This manuscript has been authored by UT-Battelle, LLC, under contract DE-AC05-00OR22725 with the US Department of Energy (DOE). The US government retains and the publisher, by accepting the article for publication, acknowledges that the US government retains a nonexclusive, paid-up, irrevocable, worldwide license to publish or reproduce the published form of this manuscript, or allow others to do so, for US government purposes. DOE will provide public access to these results of federally sponsored research in accordance with the DOE Public Access Plan (https://www.energy.gov/doe-public-access-plan).
✉e-mail: mihaela.vlasea@uwaterloo.ca

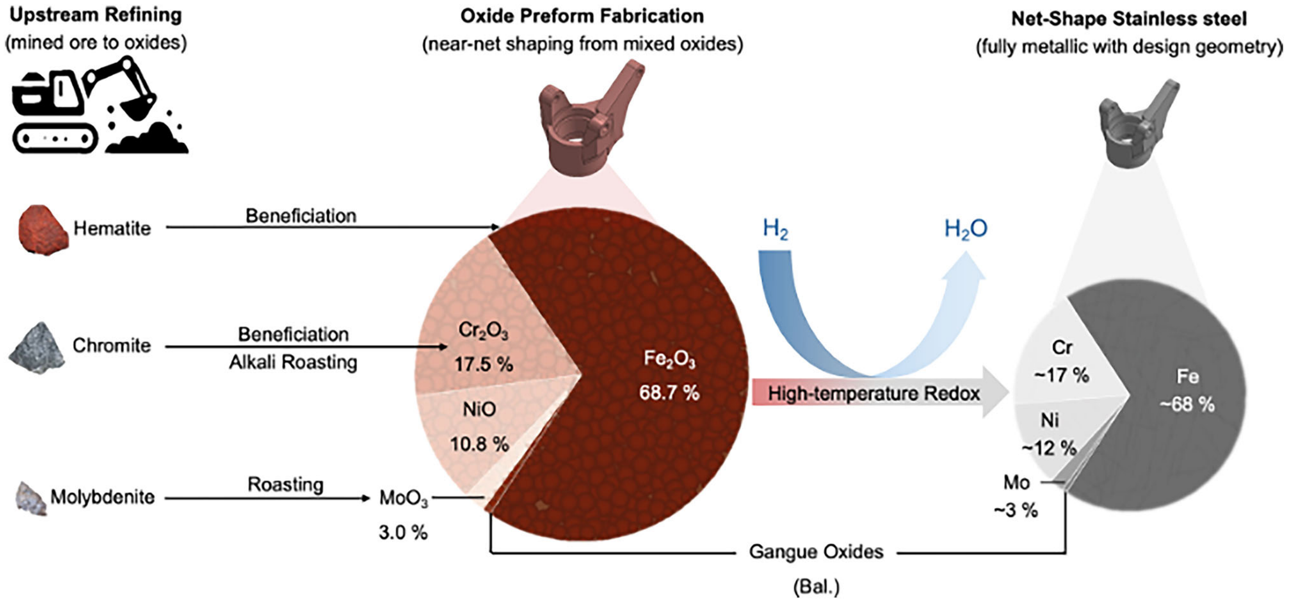

**Fig. 1** | Conceptual schematic of ore-derived oxides to net-shape stainless steel via $H_2$-based redox alloying.

**Fig. 2** | **Characterization of oxide mass and phase change upon $H_2$-based redox. a** Oxide-to-metal conversion ($\alpha$) and instantaneous mass loss ($\Delta m(t)/m_0$) derived from TGA. **b** XRD patterns before and after TGA.

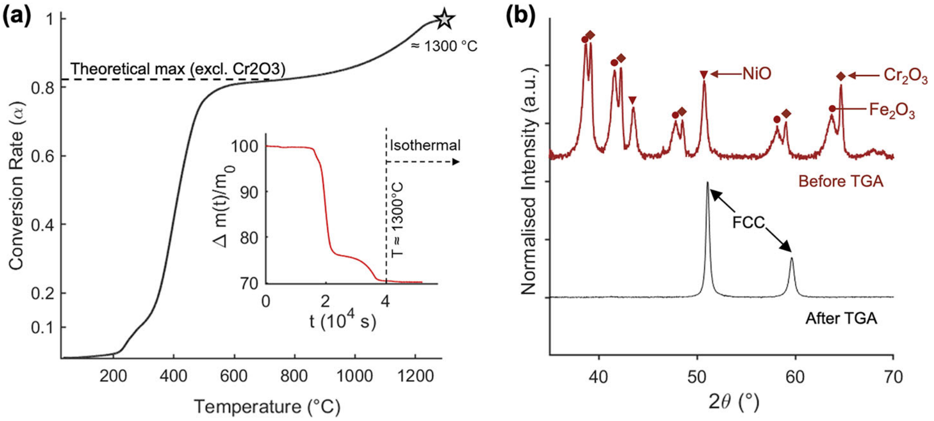

rationalize the sequential oxide reduction and alloying within mixed system using thermodynamic calculations, offering a new pathway for design oxide precursors as alloying agents.

Figure 1 outlines the proposed paradigm. The case-study alloy, austenitic stainless steel, comprises iron as the base matrix, with chromium for passivation and nickel and molybdenum for corrosion resistance. Iron and chromium are commonly derived from oxide-bearing mineral sources (e.g., hematite, chromite) that often coexists with alumina/silicate gangue partially removable via beneficiation (e.g., leaching, physical separation)[8]; alkali roasting may be used later for the subsequent extraction[9]. Molybdenum is commonly produced from molybdenite concentrates via oxidative roasting to molybdenum trioxide ($MoO_3$), which serves as the standard precursor to metallic Mo[10]. Nickel recovery is comparatively challenging because it only presented at low concentrations in lateritic or sulfidic ores[11]. Although $H_2$-based reduction of nickel sulfides is thermodynamically feasible, the presence of sulfur complicates processing[12]; therefore, nickel oxide (NiO) is used here as a simplified carrier to model nickel addition. Overall, the selected oxides serve as industrially relevant model feedstocks. These oxides are mixed and shaped into a preform with a geometry close to the final part. Upon exposure to $H_2$ and high-temperature, the preform undergoes redox-driven reactions form metallic stainless steel part. During this process, shrinkage driven by oxygen removal and porosity closure is expected; however, this dimensional change can be compensated for through design.

## Results

### Oxides-to-metal conversion

Among the transition metal oxides presented in the mixture (Supplementary Fig. S1), $Fe_2O_3$, NiO, or $MoO_3$ are unstable phases under $H_2$ below 1300 °C[13,14], while reduction of $Cr_2O_3$ is only thermodynamically feasible under carbon-based reductant at 1300 °C, as widely utilized in ferrochromium production using $CH_4$-$H_2$ mixtures[15]. Experimentally, the reducibility of the mixed oxides under $H_2$ was evaluated using a slow ramp of 1 K/min up to 1300 °C. The extent of oxides-to-metal conversion, defined as $\alpha$ = (oxygen removed)/(total oxygen initially present), was derived from TGA measurement and plotted in Fig. 2a. The $\alpha$-curve climbs to $\alpha \approx 0.81$ by 700 °C, surpassing the theoratical maximum $\alpha$ if assuming $Cr_2O_3$ remains unreduced. The inset, which displays the instantaneous mass loss rate, highlights that most of the reduction occurred rapidly below 700 °C. Above this temperature, the reduction progresses asympototically as $\alpha$ approach unity where all transition metal oxides were fully metalized when approaching 1300 °C. Ex-situ XRD patterns in Fig. 2b corroborate the complete reduction, including that of $Cr_2O_3$, and reveal a transformation from mixed oxides phases to a single set of FCC reflections. This suggests that the reduced Fe, Ni, Cr, and Mo atoms have been successfully incorporated into a solid solution, forming an austenitic matrix. EDS analysis from four scan areas of 2500 μm$^2$ across the TGA sample cross-section showed an average composition of $Fe_{68.11\pm0.43}$ $Cr_{16.74\pm0.34}$ $Ni_{12.01\pm0.25}$

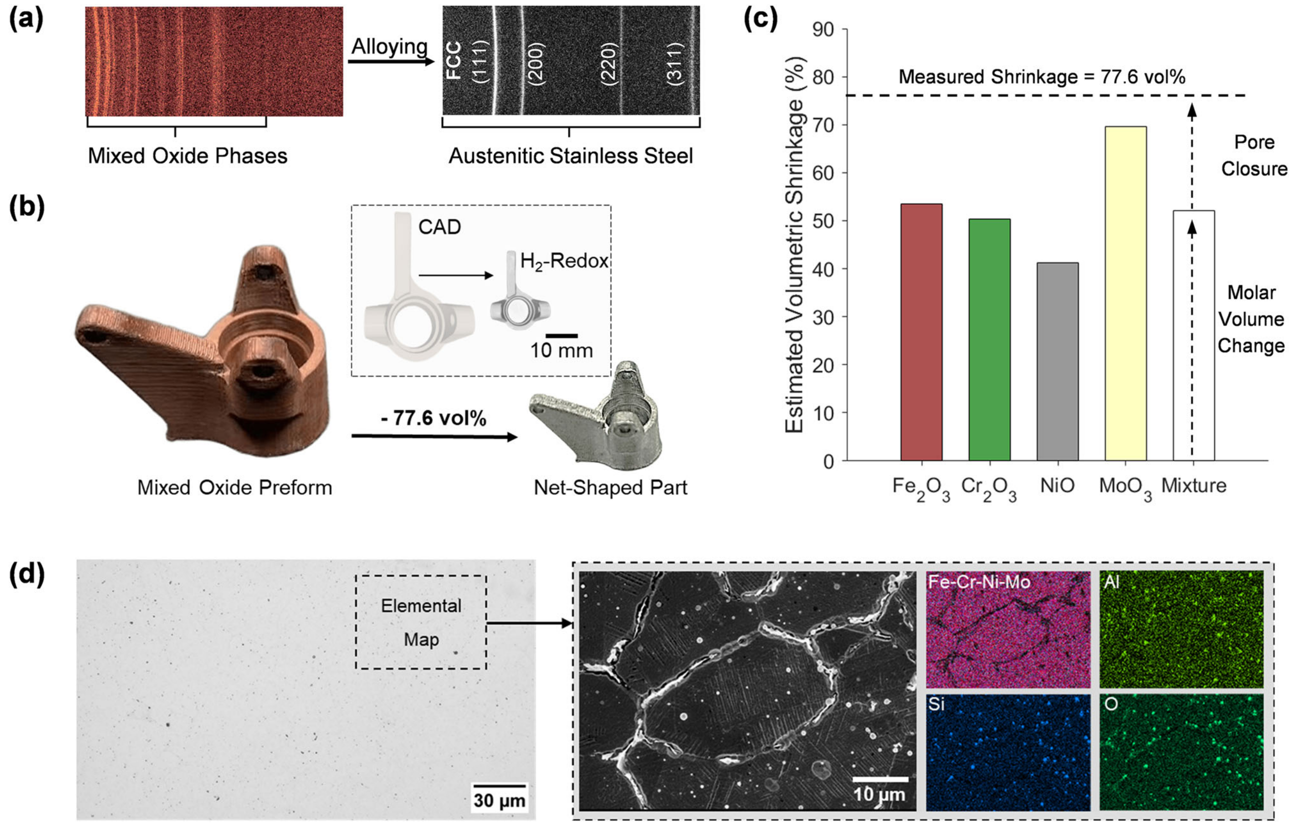

**Fig. 3 | Macro- and microstructural evolution during $H_2$-based redox alloying.** **a** X-ray diffractograms of the oxide mixture before and after $H_2$-based redox alloying in the tube furnace. **b** Photographs showing the geometrical changes of the gal-cast part. **c** Comparison between theoretical shrinkage calculated from oxide reduction and the experimentally measured value. **d** Optical micrograph (left) and SEM-EDS maps (right) showing the dense microstructure decorated by Al- and Si-based particulates.

$Mo_{2.34\pm0.61}$ (wt.%), confirming a near-complete reduction of all transition metal oxides to form the targetted $Fe_{68}Cr_{17}Ni_{12}Mo_3$.

### Macro- and micro-structural evolution

The reducibility of the oxide mixture was further evaluated using gel-cast parts processed under a tube furnace with the same heating rate (1 K/min) as in the TGA experiment. X-ray diffractograms collected from the center of the sample cross-section reaffirmed a complete transformation to a single FCC phase following $H_2$-redox (Fig. 3a), accompanied by a distinct color change from hematite red to metallic silver (Fig. 3b). Dimensional comparison against the original CAD model revealed a substantial volumetric shrinkage of 77.6% (Fig. 3c), attributable to both redox-driven volume changes and sintering-induced densification. The theoratical shrinkage due to metalization of oxides can be approximated from the molar volume ratio of the pure metal ($V_{metal}$) and its oxide ($V_{oxide}$): $1 - nV_{metal}/V_{oxide}$, where $n$ is the number of metal atoms per mole volume of oxide. Applying a composite theory (i.e., mass-weighted rule of mixtures) to the present oxide composition yields a calculated shrinkage of 52.4 vol.%, due solely to molar volume change during reduction (Fig. 3c). The remaining shrinkage is ascribed to the densification via pore closure. Notably, despite the high shrinkage observed, the final geometry exhibits isotropic shrinkage and retains the intended design.

Microstructural analysis (Fig. 3d) shows a fully-dense, crack-free matrix with grain-level uniform distribution of Fe, Cr, Ni, and Mo, as a result of $H_2$-redox alloying. However, submicron inclusions, further resolved by SEM-EDS after Kalling etching, were identified as residual Si- and Al-based gangue oxides located at boundary areas and pore interfaces. These oxides remain chemically distinct, forming no detectable compound with transition metals, as further confirmed by EDS analyses on unetched microstructure (Supplementary Materials, Figs. S2 and S3). Prior studies on $H_2$-reduced iron ores have linked the presence of Si/Al oxides to swelling and cracking due to their more than one order of magnitude thermal expansion mismatch with FCC-iron[16–18]. However, no such macroscopic defects are observed here. Nonetheless, the gangue oxides consistently coincide with residual pores or reside at interfaces, both indicative of mechanical degradtion due to stress concentration and interfacial debonding. It seems that purification of oxides to remove gangue elements are imperative if relying on ore-derived feedstock for direct net-shape manufacturing of metal components.

Collectively, these findings establish the feasibility of direct ore-to-part fabrication using $H_2$-based redox alloying, producing bulk components without geometrical deformation. However, the complete recovery of each element, specifically, Cr and Mo from their oxides under the solid-state $H_2$ sintering condition reported here, is still not well understood. Previous studies have reported significant Cr recovery (up to ~50 wt.%) from chromite ores via $H_2$ plasma smelting reduction to produce ferrochrome as the stainless steel precusor[19,20]. Such plasma-assisted processes, however, operate under non-equilibrium conditions that differ fundamentally from the thermally driven gas–solid reduction reactions relevant to the present process. To gain insight into the reduction sequence leading to the formation of the final austenitic stainless steel, thermodynamic calculations were therefore performed.

## Discussion

Firstly, equilibrium phase evolution for the ore-derived oxide mixture in $H_2$ is presented in Fig. 4a. Under equilibrium at low temperature, $Fe_3O_4$, $FeCr_2O_4$, NiO, and $MoO_2$ are stable. It is interesting to note that, none of the starting oxides, i.e., $Fe_2O_3$, $MoO_3$, $Cr_2O_3$, are stable at low temperature in the presence of $H_2$, indicating reaction between oxides to form stable products. As temperature increases, the reduction proceeds sequentially, beginning with $MoO_2 \rightarrow Mo$, followed by $NiO \rightarrow Ni$, and finally $Fe_3O_4 \rightarrow FeO \rightarrow Fe$ and $Cr_2O_3 \rightarrow Cr$. Upon formation of elemental Fe in BCC phase, subsequent

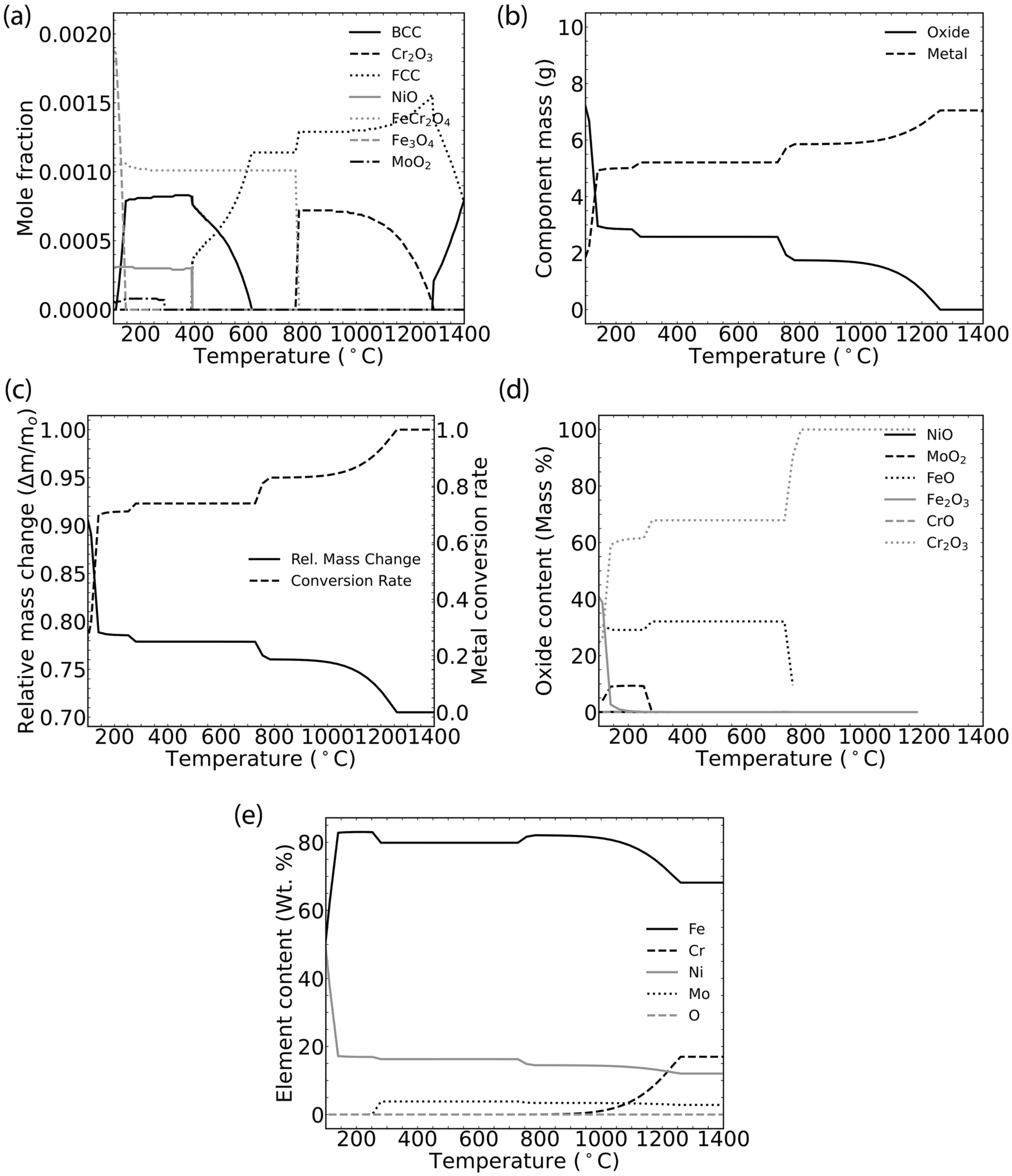

**Fig. 4 | Thermodynamic and process metallurgy calculations of oxide reduction and metal formation during $H_2$-based redox alloying.** **a** Equilibrium phase evolution for a mixture of oxide powders and excess $H_2$. **b** Process metallurgy calculation indicating amount of oxide and metal formed when considering 10 g of mixed oxides in $H_2$. **c** Relative mass change and metal conversion rate corresponding to (**b**). **d** Evolution in constitents of oxides with reduction temperature. **e** Evolution of metal composition with reduction temperature.

reduction products like Ni, Mo, and Cr dissolve progessively into the BCC of Fe matrix, ultimatly forming austenitic stainless steel (FCC phase in Fig. 4a). To quantify this reduction sequence under expreimental conditions as shown in the TGA data in Fig. 2, thermodynamic calculations were performed based on the reduction of 10 g of ore derived oxide mixture using 100 g of $H_2$ (100 g was assumed to simulate the continuous flow of $H_2$).

Figure 4b shows the evolution of oxide and metal masses as a function of temperature. Initially, the system contains 10 g of oxide. As the temperature increases, the formation of metallic species begins, accompanied by a progressive reduction in oxide mass. Approaching 1250 °C, the metal mass reaches ~ 7 g, while the oxide mass is fully depleted. Beyond 1250 °C, the masses of both metal and oxide pleateau, indicating that the completion of

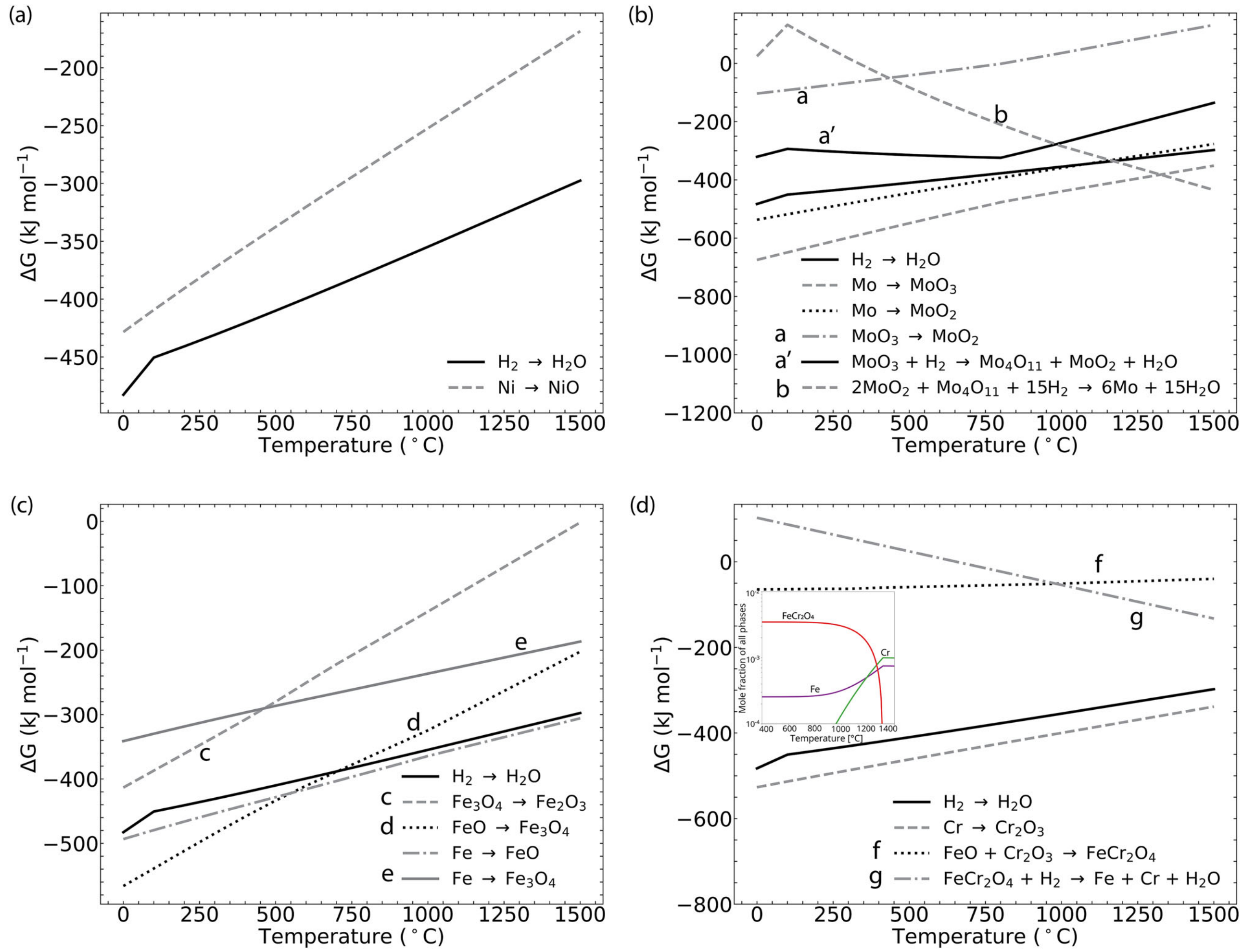

**Fig. 5 | Gibbs free energy curves for reduction reactions.** Curves showing reduction behaviour of: **a** NiO, **b** $MoO_2$, **c** $Fe_2O_3$, and **d** $Cr_2O_3$.

the reduction process. To validate the thermodynmaic simulation against the TGA data presented in Fig. 2, the relative mass change and metals conversion were calculated and are plotted in Fig. 4c. The close agreement bewteen the nature of the curve in Fig. 4c and the experimental TGA in Fig. 2b supports confidence in the thermodynamic calculations. To further resolve the reduction sequence and the composition of the metal obtained, the constituents of oxides and metal composition are shown in Fig. 4d, e, respectively. The results indicate that NiO readily reduces first, followed by $MoO_2$. The absence of $MoO_3$ in Fig. 4d suggests an immediate conversion to $MoO_2$. Subsequently, $Fe_2O_3$ reduces further into FeO, while both FeO and $Cr_2O_3$ gradually reduce as temperarure increases. This stepwise reduction is directly reflected in the evolving metallic composition shown in Fig. 4e.

From the results presented in Fig. 4, it is clear that the reduction proceeds sequentailly as NiO→Ni, $MoO_3$→Mo, $Fe_2O_3$→Fe, and finally $Cr_2O_3$ →Cr. Going purely by the Ellingham diagram[21], only the reduction of NiO→Ni by $H_2$ can be directly explained. The reduction mechanisms for the remaining oxides, necessitate further discussion.

Considering the sequential reduction of the four compounds, Fig. 5 demonstrates the thermodynamic spontaneity of their respective reduction steps. Figure 5a shows the Gibb's free enegy curves for oxidation reactions of Ni and $H_2$. The diagram clearly indicates that NiO reduction by $H_2$ is thermodynamically favorable, elucidating why Ni is the first metallic species formed during the reduction (Ref. Fig. 4e).

Figure 4a, d indicate clearly that $MoO_3$ is not a stable oxide under these conditions; instead, $MoO_2$ is thermodynamically favored. As illustrated by the Gibbs free energy curves for Mo-based oxides in Fig. 5b, that the initial reduction of $MoO_3$ to $MoO_2$ is highly favorable at low temperatures (Reaction a). This explains why $MoO_2$ is the dominant oxide phase at low temperatures, as observed in Fig. 4a, d. However, direct reduction of $MoO_2$ into Mo is thermodynamically unfavorable at low temperatures, suggesting an intermediate reduction step involving $Mo_4O_{11}$ Reaction a' in Fig. 5b. Lalik[22], using in situ neutron diffraction, have confirmed $Mo_4O_{11}$ as an intermediate oxide formed during $MoO_3$ reduction to $MoO_2$. Therefore, we propose that $MoO_3$ initially reduces to $MoO_2$ and $Mo_4O_{11}$ (Reaction a', Fig. 5b), and subsequently, the combined $MoO_2$ and $Mo_4O_{11}$ phases undergo further reduction to metallic Mo via Reaction b. The final reduction becomes thermodaynamically feasible above 280–300 °C, corresponding precisely to the observed temperature at which Mo partitions into the metallic phase in Fig. 4e. Thus, the reduction of $MoO_2$ to metallic Mo occurs fully between 280 and 400 °C.

$Fe_2O_3$ readily reduces into magnetite ($Fe_3O_4$) under $H_2$, as illustrated by Reaction c in Fig. 5c. Near approximately 400 °C, the formed $Fe_3O_4$ is further reduced to metallic Fe (Reaction e, Fig. 5c), explaining the observed increase in Fe content in the metal phase. Furthermore, above 650–700 °C, any remaining $Fe_3O_4$ can further further reduce to FeO (Reaction d, Fig. 5c), accounting for the presence of FeO observed in Fig. 4d.

Similar to $MoO_2$, $Cr_2O_3$ is challenging to reduce solely under $H_2$. However, several studies have have reported the reduction of $Cr_2O_3$ under $H_2$ at relatively lower temperatures. For example, Radomysel'sii et al.[23] investigated the co-reduction of $Fe_2O_3$ and $Cr_2O_3$ under $H_2$ targetting Fe-20Cr (wt.%) composition. They observed only trace amount of $Cr_2O_3$ after 7 h at 1100 °C and spectualted that the thermodynamic driving force originating from reduced $Fe_2O_3$ facilitated the reduction of $Cr_2O_3$. This observation underscores a critical limitation of the classical Ellingham diagram, which assumes that the activity of the metal $\alpha_{Me}$ as unity, thus it models oxidation of pure metals exclusively. In multicomponent alloy systems, where $\alpha_{Me} < 1$, the Gibbs free energy barrier for oxide reduction is effectively lowered. The equilibrium conditions for oxidation in such multicomponent systems are more accurately described by the modified relation[24]:

$$RT\, ln p_{O_2} = \mathrm{G}^{\mathrm{o}} - \frac{2a}{b} RT\, ln\, \alpha_{Me} \tag{1}$$

where $G^o$ is the standard oxidation reaction of the pure metal, and a and $b$ refer to the stoichiometry of the metal oxidation $\frac{2a}{b}\mathrm{Me} + \mathrm{O}_2 \rightarrow \frac{2}{b}\mathrm{Me}_a\mathrm{O}_b$. For instance, assuming an ideal $Fe_{68}Cr_{17}Ni_{12}Mo_3$ (wt.%) solution with $\alpha_{Me} \approx 0.18$, the driving force for $Cr_2O_3$ reduction (quantified by $\mathrm{G}^{\mathrm{o}}_{\mathrm{oxide}} - \mathrm{G}^{\mathrm{o}}_{\mathrm{H_2O}}$ value) shifts by ~ 39 kJ/mol toward spontaneity. Similarly, more recent study conducted by Shankar et al.[25] reported that in mixed oxide systems, the reduced activity of Cr in the metallic phase could aid in lowering the reduction temperature of $Cr_2O_3$.

From the perspective of lowering thermodynamic barrier for such reaction, we propose an additional mechanism to explain the observed low temperature reduction of $Cr_2O_3$. As previously discussed for $Fe_2O_3$, residual $Fe_3O_4$ can undergo reduction into FeO beyond 600 °C (Reaction d, Fig. 5c), with the presence of FeO further supported by thermodynamic calculations in Fig. 4d. FeO and $Cr_2O_3$ can react to form spinel based $FeCr_2O_4$ via Reaction f in Fig. 5d, which is thermodynamically favorable, as indicated by the equlibrium calculations in Fig. 4a. The $FeCr_2O_4$ spinel can undergo reduction to metallic Fe and Cr via Reaction g in Fig. 5d. It should be noted that this reaction is thermodynamically feasible above ~ 1000 °C, corresponding to the temperature range where Cr partition into the metallic phase is observed. Furthermore, the inset in Fig. 5d confirms that the reduction of $FeCr_2O_4$ under $H_2$ becomes thermodynaimcally favorable above 1000 °C, with the complete reduction achieved close to 1280 °C.

In summary, we demonstrate that using ore derived oxides as feedstock for additive manufacturing, followed by sintering under $H_2$ atmosphere is a viable manufacturing route to tranform extracted ore into near-net-shape parts. We demonstrate this concept using mixed oxide system comprising $Fe_2O_3$, $Cr_2O_3$, NiO, and $MoO_3$ to fabricate bulk near-net-shaped austenitic stainless steel part. Based on experimental and thermodynamic results, the following conclusions can be drawn:

(i) $H_2$-based redox directly transforms sustainable oxide preforms into net-shape bulk metal parts. Alloying and densification can proceed even in the presence of minor Al and Si-based gangue impurities; however, these impurities tend to reside within residual pores and at interfaces. Shrinkage during oxide metalization is significant but uniform, in constrast to classical powder sintering where differential shrinkage often leads to slumping and distortion.

(ii) Phase transformations between oxides within the mixed system can alter the reduction pathway and lower the reduction temperature relative to pure single oxides, thererby assisting in the reduction of otherwise difficult-to-reduce under $H_2$. We propose this mechanism as the main pathway for the reduction of $MoO_3$ and $Cr_2O_3$ during the formation of austenitic stainless steel.

(iii) Complete reduction of difficult-to-reduce oxides by exploiting oxide-to-oxide phase transformation can open up new avenues in $CO_2$-free steel production and on-the-fly alloying and can potentially provides a pathway to reduce refractory oxides (Nb, W, and V) with comparable stability under $H_2$.

Together, these findings lay the foundation for utilization metallic ores as of sustainable, low-cost feedstocks for direct net-shape metal manufacturing.

## Methods

### Near-net-shape manufacturing of oxide mixture

For our investigation, micronized $Fe_2O_3$ (KREMER Pigmente, $D_{90} = 5.91$ µm), $Cr_2O_3$ (KREMER Pigmente, $D_{90} = 3.42$ µm), NiO (Alfa Aesar, 400 mesh), and $MoO_3$ (Sigma Aldrich, ~100 nm) powders were blended to target a nominal composition of 316 grade austenitic stainless steel (17Cr–12Ni–3Mo–68Fe (wt.%)) after complete oxide reduction (Fig. 1). The oxide mixture was homogenized via low-energy ball milling (250 rpm, 4 h, ball-to-powder ratio 10:1), then shaped into a suspension bearing using gel-casting following established protocols described in ref. 26. Gangue impurities were introduced through the $Fe_2O_3$ pigment, contributing 0.34 wt.% Si and 0.36 wt.% Al.

### Oxide reduction experiments

Redox test of the oxide mixture (without binder) was performed using thermogravimetric analysis (TGA; STA 449F3, Netzsch). A sample mass of 107.41 mg was subjected to a flowing $H_2$ atmosphere (99.999% purity, Linde AG) at 100 mL/min. The thermal profile consists of heating at 1 °C/min to 1300 °C, followed by a 2 h of isothermal hold. The measurement was repeated under identical conditions. Redox test of gel-casted demonstrators was conducted in a tube furnace (Elektromat Dresden) under flowing $H_2$ at 2.5 L/min. A debinding step was first performed at 500 °C for 1 h, followed by redox processing using the same thermal profile as employed in the TGA experiments.

### Macro- and micro-structural characterizations and analysis

Post-reduction geometries were measured using a contact-free optical scanner (ALCON, Hexagon) and compared with the original computer-aided design (CAD) model to quantify volumetric shrinkage (vol%) and evaluate geometrical distortion. Phase analysis of the ball-milled mixture and redox specimens were conducted via X-ray diffraction (XRD; D8 DISCOVER, Bruker) using a Cobal source (Co-Kα, λ = 1.79026 Å), operated at 40 kV and 45 mA. Microstructural analaysis was carried out using a field emission scanning electron microscopy (FESEM; Leo 1530, Zeiss) equipped with an energy dispersive spectroscopy (EDS) detector. Thermodynamic calculations presented were performed using TCOX10 oxides database of ThermoCalc in conjunction with the Process Metallurgy module of ThermoCalc[27,28].

## Data availability

The datasets generated and/or analyzed during the current study are available within the article. Any additional data apart from what is provided are available from the corresponding author on reasonable request.

Received: 3 September 2025; Accepted: 21 January 2026;
Published online: 02 March 2026

## References

1. Raabe, D. The materials science behind sustainable metals and alloys. *Chem. Rev.* **123**, 2436–2608 (2023).
2. Norgate, T. & Rankin, W. The Role of Metals in Sustainable Development. *Green Processing 2002 - Proceedings: International Conference on the Sustainable Proceesing of Minerals* (2002).
3. Wang, R. R., Zhao, Y. Q., Babich, A., Senk, D. & Fan, X. Y. Hydrogen direct reduction (H-DR) in steel industry—An overview of challenges and opportunities. *Clean. Prod.* 329, https://doi.org/10.1016/j.jclepro.2021.129797 (2021).
4. Wei, S., Ma, Y. & Raabe, D. One step from oxides to sustainable bulk alloys. *Nature* **633**, 816–822 (2024).
5. Zhang, D., Kenel, C. & Dunand, D. C. Microstructure and mechanical properties of 3D ink-extruded CoCrCuFeNi microlattices. *Acta Mater.* **238**, 118187 (2022).
6. Kenel, C., Davenport, T., Li, X., Shah, R. N. & Dunand, D. C. Kinetics of alloy formation and densification in Fe-Ni-Mo microfilaments

extruded from oxide- or metal-powder inks. *Acta Mater.* **193**, 51–60 (2020).

7. Purohit, S., Pownceby, M. I. & Guiraud, A. Sticking and swelling of iron ore pellets: Mechanisms and controlling factors. *J. Sustainable Metallurgy* https://doi.org/10.1007/s40831-024-01000-3 (2025).
8. Nikolaeva, N. V., Aleksandrova, T. N., Chanturiya, E. L. & Afanasova, A. Mineral and Technological Features of Magnetite-Hematite Ores and Their Influence on the Choice of Processing Technology. *ACS Omega* **6**, 9077–9085 (2021).
9. Murthy, Y. R., Tripathy, S. K. & Kumar, C. R. Chrome ore beneficiation challenges & opportunities – A review. *Min. Eng.* **24**, 375–380 (2011).
10. Lasheen, T. A., El-Ahmady, M. E., Hassib, H. B. & Helal, A. S. Molybdenum Metallurgy Review: Hydrometallurgical Routes to Recovery of Molybdenum from Ores and Mineral Raw Materials. *Miner. Process. Extr. Metall. Rev.* **36**, 145–173 (2015).
11. Manzoor, U., Mujica Roncery, L., Raabe, D. & Souza Filho, I. R. Sustainable nickel enabled by hydrogen-based reduction. *Nature* https://doi.org/10.1038/s41586-025-08901-7 (2025).
12. Wang, F., Marcuson, S., Elsawi, R., Liu, L. & Barati, M. Effect of hydrogen on nickel extraction from low-grade ultramafic nickel sulfide concentrate. *Int. J. Hydrogen Energy* **158**, 150506 (2025).
13. Özgün, Ö, Dirba, I., Gutfleisch, O., Ma, Y. & Raabe, D. Green Ironmaking at Higher H 2 Pressure: Reduction Kinetics and Microstructure Formation During Hydrogen - Based Direct Reduction of Hematite Pellets. *J. Sustain. Metall.* **10**, 1127–1140 (2024).
14. Rukini, A., Rhamdhani, M. A., Brooks, G. A. & Bulck, A. Van Den. Metals Production and Metal Oxides Reduction Using Hydrogen: A Review. *J. Sustain. Metall.* **8**, 1–24 (2022).
15. Anacleto, N. & Ostrovski, O. Solid-state reduction of chromium oxide by methane-containing gas. *Metall. Mater. Transac. B.* **35**, 609–615 (2004).
16. Ma, Y. et al. Hierarchical nature of hydrogen-based direct reduction of iron oxides. *Scripta Mater.* **213**, 114571 (2022).
17. Moukassi, M., Gougeon, M., Steinmetz, P., Dupre, B. & Gleitzer, C. Hydrogen reduction of wustite single crystals doped with Mg, Mn, Ca, Al, and Si. *Metall. Transac. B* **15**, 383–391 (1984).
18. Lei, J. et al. Mechanism study on gas-based reduction swelling behavior of ultra-high grade pellets. *J. Mater. Res. Technol.* **26**, 823–836 (2023).
19. Taimullah, A. et al. Direct and sustainable stainless steelmaking from nickel and chromite ores by hydrogen plasma smelting reduction. *Int. J. Miner., Metall. Mater.* **32**, 1881–1892 (2025).
20. Tandersen, D. et al. Rapid and Sustainable Ferrochrome Production from Chromite Ore by Hydrogen Plasma Smelting Reduction. *Plasma Chem. Plasma Process.* **45**, 1045–1062 (2025).
21. Shang, S. L., Lin, S., Gao, M. C., Schlom, D. G. & Liu, Z. K. Ellingham diagrams of binary oxides. *APL Mater* **12**, 081110 (2024).
22. Lalik, E. Kinetic analysis of reduction of MoO3 to MoO2. *Catal. Today* **169**, 85–92 (2011).
23. Radomysel, I. D., Barshohevskaya, L. F. & Ya Dzykovich, I. Process of coreduction of iron and chromium oxides with hydrogen ii. mechanism of the reduction process. *Theory, production technology, and properties of powders and fibers* (1971).
24. Epifano, E. & Monceau, D. Ellingham diagram: A new look at an old tool. *Corros Sci* **217**, (2023).
25. Shankar, S. et al. Unraveling the Thermodynamics and Mechanism behind the Lowering of Reduction Temperatures in Oxide Mixtures.
26. Weissgaerber, T. et al. Review of Sinter-Based Additive Manufacturing (SBAM) - Status and Prospects. *J. Japan Soc. Powder* **72**, S321–S326 (2025).
27. APPLICATIONS OF THERMO-CALC Process Metallurgy. https://thermocalc.com/solutions/solutions-by-application/process-metallurgy/.
28. Metal Oxide Solutions Database. https://thermocalc.com/products/databases/metal-oxide-solutions/.

## Acknowledgements

The authors would like to acknowledge the financial support from Federal Economic Development Agency for Southern Ontario, Regional Innovation Ecosystem, Canada, grant 814654. The authors would like to acknowledge Fraunhofer IFAM for providing raw materials and facilities used for this study. The first author would like to express appreciation for the Natural Sciences and Engineering Research Council of Canada (NSERC) Canada Graduate Scholarships—Doctoral Award (CGS-D).

## Author contributions

M.Y. (Conceptualization; Formal analysis; Lead; Investigation; Methodology; Visualization; Writing—original draft; Writing—review & editing). R. K. (Formal analysis; Investigation; Visualization; Writing—original draft). M. K. (Investigation; Supporting; Visualization; Writing—review & editing). M. V. (Funding acquisition; Project administration; Supervision; Writing—review & editing). All authors reviewed and approved the manuscript for submission.

## Competing interests

The authors declare no competing interests.

## Additional information

**Supplementary information** The online version contains supplementary material available at https://doi.org/10.1038/s44334-026-00069-w.

**Correspondence** and requests for materials should be addressed to Mihaela Vlasea.

**Reprints and permissions information** is available at http://www.nature.com/reprints

**Publisher's note** Springer Nature remains neutral with regard to jurisdictional claims in published maps and institutional affiliations.

**Open Access** This article is licensed under a Creative Commons Attribution-NonCommercial-NoDerivatives 4.0 International License, which permits any non-commercial use, sharing, distribution and reproduction in any medium or format, as long as you give appropriate credit to the original author(s) and the source, provide a link to the Creative Commons licence, and indicate if you modified the licensed material. You do not have permission under this licence to share adapted material derived from this article or parts of it. The images or other third party material in this article are included in the article's Creative Commons licence, unless indicated otherwise in a credit line to the material. If material is not included in the article's Creative Commons licence and your intended use is not permitted by statutory regulation or exceeds the permitted use, you will need to obtain permission directly from the copyright holder. To view a copy of this licence, visit http://creativecommons.org/licenses/by-nc-nd/4.0/.

© The Author(s) 2026